Journal of Materials Chemistry C

ROYAL SOCIETY OF CHEMISTRY

PAPER

View Article Online
View Journal | View Issue

Cite this: J. Mater. Chem. C, 2025, 13, 14301

Insights into the thermal decomposition and conversion mechanism of nickel xanthates to nickel sulfides†

Melissa Sophie Egger, [a] Marco Sigl, [a] Robert Saf, [a] Heinz Amenitsch, [b] Ana Torvisco, [b] Thomas Rath *[a] and Gregor Trimmel *[a]

Metal sulfides are promising materials for a wide range of applications, from environmental applications to energy conversion and storage. Like many other transition metal sulfides, nickel sulfide exists in different stoichiometries and phases, which influence their chemical and physical properties. While this feature enables the compound's diversified applications, it also makes it necessary to develop simple and reproducible methods to prepare nickel sulfide with defined composition, phase, and morphology. For metal xanthates, the design of the xanthate ligand allows to tune the properties of the metal sulfide obtained by their thermal conversion. To efficiently tailor the precursor to the application, it is imperative to understand the degradation mechanism of the precursors and the formation of the nickel sulfide phases. In this study, we synthesized a series of nickel xanthates bearing alkyl side chains of varying lengths and branching: methyl, ethyl, *n*-propyl, iso-propyl, iso-butyl, *n*-pentyl, neo-pentyl, and *n*-hexyl. Together with two additional nickel xanthates, we systematically investigated their thermal decomposition behavior and the resulting decomposition products using thermogravimetric analysis with coupled gas chromatography/mass spectrometry, pyrolysis gas chromatography/mass spectrometry, single crystal and powder X-ray diffraction, and grazing incidence wide angle X-ray scattering. Based on these findings, we propose a two-step decomposition mechanism that combines alkyl transfer between the ligands with an extended version of the literature-known Chugaev mechanism, which describes alkene formation from xanthates. This refined mechanism can explain the conflicting degradation products reported in literature so far. Additionally, we studied the influence of the ligand on the formed nickel sulfide using temperature dependent X-ray scattering experiments. The decomposition of the xanthates leads to the initial formation of α-NiS at low temperatures for all the precursors, followed by a phase transformation at higher temperatures. Depending on the precursor both pure α- or β-NiS and various mixed phases can be obtained.

Received 13th March 2025,
Accepted 25th May 2025

DOI: 10.1039/d5tc01096a

rsc.li/materials-c

Introduction

Transition metal sulfides are a broad and versatile class of inorganic semiconductors. They have a wide scope of applications like photocatalysis,[1,2] electrocatalysis,[3] (opto-) electronic devices,[4–6] energy storage and conversion materials.[7] Favorable properties such as high photosensitivity, lower band gaps than metal oxides, high specific capacities, and a high degree of versatility in terms of crystallinity, composition, and morphology, make metal sulfides a promising class of compounds for the development of future-oriented technologies.[1,7,8]

Nickel sulfide is an inorganic semiconductor which presents itself in a multitude of stoichiometries and crystalline phases. Depending on the specific phase, its scope of applications is vast: From energy storage applications such as battery or supercapacitor electrodes,[9] photo(electro)catalytic water splitting,[10,11] to medicinal applications[12,13] or water treatment and disinfection.[14] Nevertheless, it is necessary to devise simple, economical and reliable methods to control stoichiometry, polymorphs and morphology.[8]

There are numerous methods for the preparation of binary, ternary or other multi-metal sulfide nanomaterials. The different obtainable structures such as nanospheres (0D), nanorods (1D), nanosheets (2D) and mesoporous hierarchical structures (3D) strongly influence nanostructured materials and their

[a] Institute for Chemistry and Technology of Materials (ICTM), NAWI Graz, Graz University of Technology, Stremayrgasse 9, 8010 Graz, Austria. E-mail: thomas.rath@tugraz.at, gregor.trimmel@tugraz.at
[b] Institute of Inorganic Chemistry, NAWI Graz, Graz University of Technology, Stremayrgasse 9, 8010 Graz, Austria

† Electronic supplementary information (ESI) available: NMR spectra, additional single crystal structures, mass spectrometry data, additional GIWAXS data of heating run experiments. CCDC 2430036–2430039. For ESI and crystallographic data in CIF or other electronic format see DOI: https://doi.org/10.1039/d5tc01096a

functional properties.[15] However, to enable the use of nanostructured metal sulfides, large-scale synthesis methods of metal sulfides with well-defined, tunable properties are necessary.[1]

The most commonly used preparation methods for transition metal sulfide nanostructures are hydro- or solvothermal synthesis. By varying reactants (metal precursor, sulfur source, surfactant, solvent) and conditions (reaction time and temperature, concentrations, pH-values) these methods provide good control over the nanostructure morphology and composition.[16] A promising alternative to conventional solvothermal synthesis methods is the use of single source precursors (SSPs). This approach uses metal complexes with ligands containing the desired chalcogenide. SSPs can be used in a broad range of different fabrication methods to replace multiple precursors. Volatile SSPs can be used in molecular organic chemical vapor deposition, which provides clean decomposition at relatively low temperatures. Soluble SSPs might be used in further methods such as aerosol-, spray-, or injection pyrolysis, in the solvothermal preparation of nanoparticles, or also directly in solvent-free solid-state pyrolysis. Both elements being present in a single compound simplifies the experimental procedure for the fabrication of metal sulfides compared to using multiple element sources.[18] Furthermore, the ligand usually coordinates to the metal center *via* the chalcogenide. Therefore, the precursor features preformed bonds between the metal and the chalcogen atoms, which can result in a product with fewer defects and more defined stoichiometry. Additionally, this approach allows not only the control of the stoichiometry but also the control of other properties such as solubility and volatility of the precursor by the design of the ligand.[17,18]

There are a few characteristics necessary for a compound to be suitable as a SSP. The synthesis should be simple, easily scalable and the compound should be obtained in high yields and high purity to prevent possible contaminations of the deposited material. The precursor should be stable in air, have a low toxicity, and, ideally, the thermal decomposition of the complex should yield the thin film/nanoparticles with only volatile byproducts. However, the ligands are often not cleanly evaporating into the gas phase, but undergo complex fragmentations, especially for heteroleptic compounds. For the rational design of precursors yielding materials with the desired properties, insights into the molecular decomposition pathways are necessary.[18]

One class of single-source precursors for the fabrication of metal sulfide nanoparticles or thin films are transition metal xanthates.[19–27] Metal xanthates are the metal salts of xanthic acid, therefore already containing metal–sulfur bonds, and are highly versatile as precursors through the modification of the ligands. Metal xanthates are both easily synthesized and easily converted thermally to the corresponding metal sulfide. The thermolysis occurs at relatively low temperatures with only volatile byproducts, and can be done solventless, or in different media such as solvents or polymers.[28] The xanthate's properties can be modified *via* the choice of the alkyl side chain of the xanthate ligand(s),[22,29,30] or by using heteroleptic complexes containing additional ligands such as triphenylphosphine[31] or

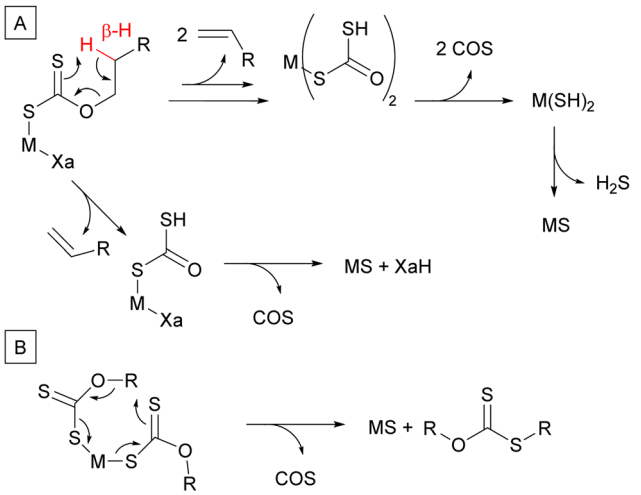

Scheme 1 (A) Chugaev-like degradation pathway for metal xanthates forming the metal sulfide and COS, alkene and xanthic acid side products. (B) Degradation pathway for xanthates proposed by A. Piquette, yielding a purely organic xanthate *via* an alkyl transfer.[2]

pyridine derivatives.[32,33] The modification of volatility and solubility enables the use in different processing methods such as aerosol-assisted chemical vapor deposition, spin coating, drop casting, and co-casting with other metal xanthates or polymers.[18,34,35] This allows using xanthates in quite interesting and unconventional applications, one of which is laser printing of xanthates on paper using a mixture of metal xanthate, polymer and commercial toner. Thermal conversion of the precursor in the toner mixture yields metal chalcogenides for printed electronics.[34] Another application is to prepare polymer thin films containing xanthate based semiconductor nanostructures for flexible electronics.[36]

However, the decomposition pathway of metal xanthates, often stated to occur in a Chugaev- or Chugaev-like mechanism (Scheme 1A), is rather complicated. Previous research suggests that the identity of the metal center has only a small influence on the pathway. On the other hand, major differences in the produced byproducts, and therefore the corresponding pathway, were found depending on the alkyl substituent. An alternative pathway was proposed by A. Piquette (Scheme 1B),[21] however, the proposed eight-membered cyclic transition state is energetically unfavored and thus very unlikely. Also, this does not account for results of different studies finding the decomposition products expected for the Chugaev-elimination.[33] This highlights the need for an in-depth investigation to shed light on the complex decomposition pathway.

Consequently, in this study we prepared a series of nickel xanthates (NiXas) with ligands featuring alkyl chains of differing lengths and branching and studied the decomposition of the xanthates and the properties of the formed nickel sulfide thin films. We characterized the thermal decomposition behavior of the xanthates using thermogravimetric analysis (TGA), TGA-gas chromatography/mass spectrometry (GCMS) and pyrolysis-GC-HRMS, with the focus of this work placed on the decomposition mechanism of the nickel xanthates. Furthermore, we studied the properties of the nickel sulfide thin films using X-ray diffraction

(XRD) and temperature dependent grazing incidence wide angle X-ray scattering (GIWAXS).

Results and discussion

Synthesis and characterization

We performed the synthesis of a series of nickel *O*-alkyl dithiocarbonates (alkyl: methyl (NiXaC1),[37,38] ethyl (NiXaC2),[38–42] *n*-propyl (NiXaC3),[38,41,43] iso-propyl (NiXaC3b, b = branched),[38,40,43] iso-butyl (NiXaC4b),[37,38,40] *n*-pentyl (NiXaC5),[38,40] neo-pentyl (NiXaC5b),[44] and *n*-hexyl (NiXaC6)[37,38]) according to previously published procedures.[29,33] In addition, nickel xanthates with 2-neo-hexyl (NiXaC6b)[22] and neo-heptyl (NiXaC7b)[22] alkyl chains are investigated in this study. The synthesis route of the precursors is robust and straightforward: the potassium xanthates are synthesized from the corresponding alcohols in a quasi solvent-free synthesis, as the liquid alcohols also function as solvents. Only the solid educt neopentanol required previous dissolution of the alcohol in THF. Both the metal salts and the potassium xanthates are water-soluble, mixing the solutions at room temperature yields the water-insoluble nickel xanthates. The purification is done by simple recrystallization, and all precursors except NiXaC1 are stable in air. For NiXaC1, a significant change in the TGA profile hints at a partial degradation of the precursor after approximately one month.

The solubility of the nickel xanthates can be tuned easily by the choice of the alkyl chain. The solubility in chloroform of the precursor with the shortest possible alkyl chain, NiXaC1, is too low to prepare films. With increasing chain length, the solubility increases, and for NiXaC2 the solubility is already sufficiently high (>0.1 mmol mL^{-1}) to use this precursor for the preparation of thin films.

The procedure and the structures of the prepared xanthates are given in Scheme 2. With the exception of NiXaC5b, for which only a pyridine adduct has been reported,[44] the discussed nickel xanthates are already known in the literature. However, NMR spectra (not reported: NiXaC1, NiXaC3, NiXaC5b, NiXaC6) and crystal structures (not reported: NiXaC5, NiXaC5b) have not been published for all compounds so far. The ^{1}H and ^{13}C NMR spectra (Fig. S1–S8) given in the ESI† are in accordance with the proposed structures, as well as with the values given for the already literature known compounds.[22,39,40]

Single crystal X-ray studies

We obtained the crystal structure of the complex NiXaC5b by single crystal X-ray diffraction (see Fig. 1). The sulfur atoms of the neopentyl xanthate ligands are coordinated to the nickel in a slightly distorted square-planar geometry (Fig. 1A). The Ni–S bonds exhibit a slight shortening in *trans* arrangement, possibly due to the delocalized double bond between the bidentate ligand and the nickel center. The atoms from the dithiocarbonate moieties (–OCS$_2$–) are in one plane with the nickel center atom. Intermolecular C–H···S interactions and C–H···Ni anagostic interactions form a layered 2D-sheet structure. The anagostic interactions of the nickel center atom with two

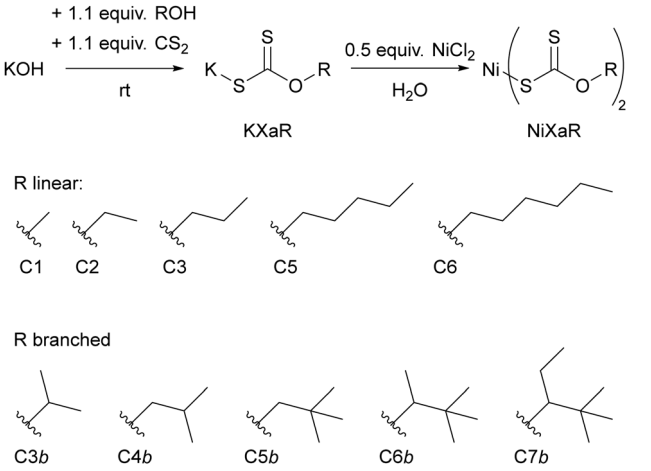

Scheme 2 Synthesis route used for the preparation of the nickel xanthates and the chemical structures of the alkyl ligands of the xanthates investigated in this study.

hydrogen atoms *trans* to each other leads to the formation of a quasi-octagonal coordination geometry around the metal center. Similar behavior could be observed for most of the other investigated complexes (NiXaC3b, NiXaC4b, NiXaC6). Only the NiXaC3 complex showed a stronger distorted geometry, with all four Ni–S bonds exhibiting different lengths, and a displacement of the nickel center out of the plane formed by the sulfur atoms. This is in accordance with the structure reported by Hoskins *et al.*,[45] and was also observed for the NiXaC1 complex.[37]

Thermogravimetric analysis

We studied the thermal decomposition behavior of the synthesized nickel xanthates using TGA as depicted in Fig. 2 (Table S1, ESI†). All investigated complexes show a one-step decomposition with the onset temperature strongly influenced by the length and branching of the alkyl chain, which has also been reported by Cavell *et al.*[38] The xanthates with linear alkyl chains (Fig. 2A) show decompositions over a narrow range. The onset temperatures (tangent method) and end temperatures increase with increasing chain length (Fig. 2C, pink). In contrast the decomposition range of the branched xanthates (Fig. 2B) is significantly broader and the onset temperatures do not correlate with the chain length (Fig. 2C, blue). The melting points given in Fig. 2C show that the crystal structure cannot be used to obtain information about the degradation behavior. For most of the nickel xanthates, the melting point is far below the onset of the degradation, and the degradation therefore occurs from the melt. An exception from this behavior is the NiXaC6b precursor, for which the melting occurs while the compound has already started to decompose. During the melting point determination this was observed as smoke evolution, followed by liquification and simultaneously continuing decomposition. For NiXaC1, we could not observe a melting point, the degradation occurred from the solid precursor as well.

The experimental mass loss for most of the xanthates is consistent with the theoretical mass loss expected for the

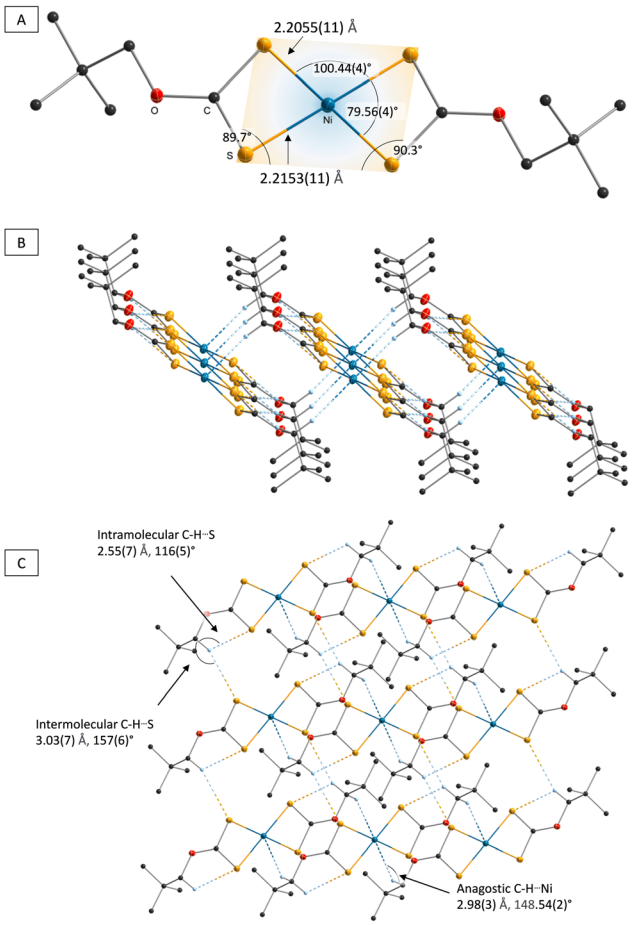

Fig. 1 (A) Crystal structure for NiXaC5b, with the view along *b*- (B) and *c*-axis (C). The compound NiXaC5b crystallizes as 3D network propagated by C–H···S hydrogen bonds and C–H···Ni anagostic interactions. All non-carbon atoms shown as 30% shaded ellipsoids. Hydrogen atoms not involved in intermolecular interactions omitted for clarity. Ni–S bonds form a slightly distorted square planar coordination (A). Each Ni center is involved in two anagostic C–H···Ni interactions *trans* to each other forming a H···Ni···H angle of 180°. Inter- and intramolecular C–H···S interactions form a S···H···S angle of 87.33°.

formation of stoichiometric NiS (see also Table S1, ESI†). Minor deviations from the theoretical value were in the range of ±2.5% pt. While a slightly lower mass loss can be explained by the presence of decomposition products or sulfates, the higher mass loss might stem from a vapor phase transport of the nickel xanthate or the newly formed nickel sulfide. The observed formation of very thin films on adjacent surfaces supports this explanation, as also observed by A. Piquette.[21]

Characterization of degradation products

The thermal decomposition of metal xanthates is generally presumed to occur in a Chugaev-like elimination reaction (Scheme 1B). This pathway proceeds *via* a 6-membered cyclic transition state of a single xanthate ligand, and yields the corresponding alkene and carbonyl sulfide (COS) as main byproducts, as well as xanthic acid.[46] Further decomposition products (such as thiol) might then be formed by the decay of the unstable xanthic acid. However, the Chugaev pathway requires the presence of a β-hydrogen in the side chain, which two of the investigated xanthates (NiXaC1 and NiXaC5b) do not possess (Scheme 3A). This indicates that the decomposition of the nickel xanthates might occur *via* different pathways.

To investigate these proposed pathways, we performed TGA-GC-MS experiments. In this setup, the TGA sample chamber is connected to the GC inlet *via* a heated transfer line. Therefore, the setup introduces some delay between the formation of the decomposition products and the start of the GC measurement. First experiments with this setup yielded ambiguous results that varied strongly between repeated measurements. A result common to all experiments was that the alkene expected from the Chugaev mechanism was usually not the main product and, in some cases, hardly present. Additionally, we found a range of decomposition products which cannot be explained by the proposed pathway, such as *O*,*S*-dialkyl dithiocarbonate, dialkyl sulfide, or CS_2.

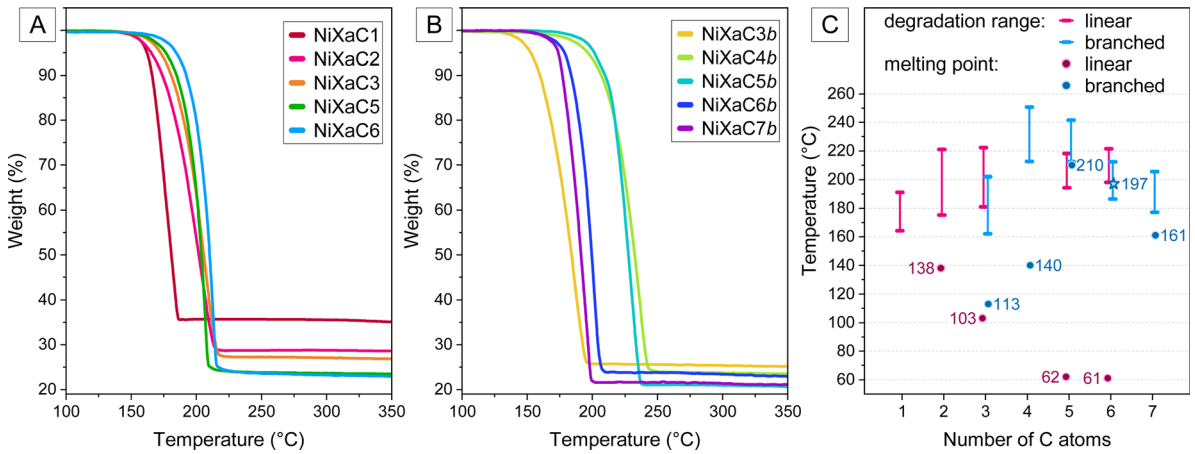

Fig. 2 TGA curves for the nickel xanthate precursors with linear (A) or branched side chains (B). Onset was determined by the tangent method. (C) Decomposition temperature ranges and melting temperatures for nickel xanthate precursors with different linear and branched side chains. Pink: linear side chains, blue: branched side chains.

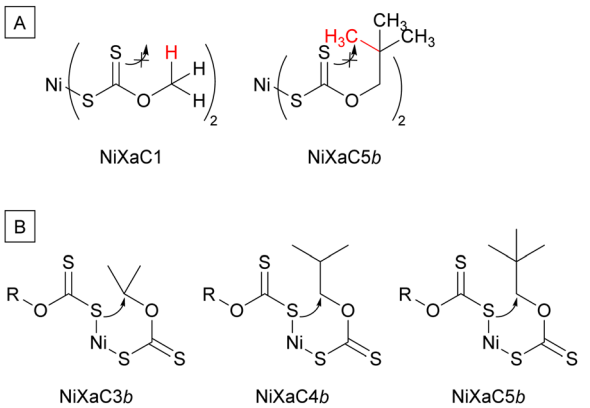

Scheme 3 (A) Synthesized compounds without β-hydrogen (nickel methyl- and neopentyl xanthate). (B) Xanthates with branched alkyl substituents (NiXaC3b, NiXaC4b and NiXaC5b) investigated by pyrolysis-GC-HRMS.

Pyrolysis-GC-HRMS

Due to the ambiguity of the results of the TGA-GC-MS measurements, we conducted pyrolysis-GC-HRMS experiments with high sensitivity and mass accuracy. In addition, the almost instantaneous sample injection to the GC-HRMS after the pyrolysis minimizes the occurrence of secondary decomposition reactions. This allows us to determine the very first decomposition steps. The GC traces of the pyrolysis-GC-HRMS experiments are given in Fig. 3 (A: linear, B: branched). The retention times and the mass spectra of the compounds are given in the ESI† (Tables S2–S9 and Fig. S9–S16).

As depicted in Fig. 3, we observed strongly dissimilar results for the linear and branched xanthates. While the linear xanthates (Fig. 3A and C) behaved similarly among each other, the branched xanthates (Fig. 3B and D) strongly differed from them and among each other. For the linear xanthates, the *O*,*S*-dialkyl dithiocarbonate (xanthate ester) species was by far the major product with 75 to 85%. The full report of the decomposition products is given in Table S10 in the ESI.† For most precursors no significant amount of alkenes was detected. In the case of NiXaC5b, where the formation of alkenes is not possible, dimethyl cyclopropane was found.

The observed decomposition products cannot be explained by the Chugaev pathway. This, as well as the absence of alkenes, instead suggests the occurrence of an alkyl transfer between the xanthate ligands, thereby forming the ester (Scheme 1B), as described by A. Piquette.[21] 8-membered transition states are usually energetically unfavorable, therefore we propose an alternative mechanism for the alkyl transfer proceeding *via* a

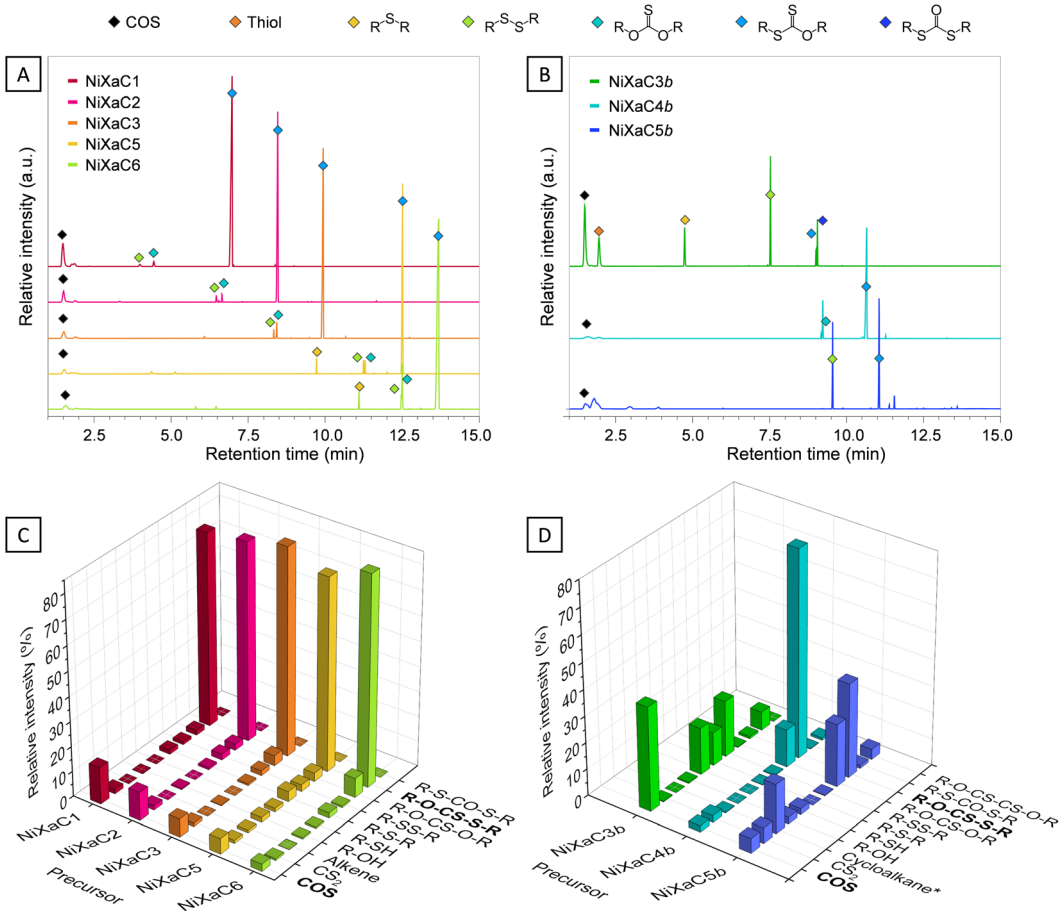

Fig. 3 Pyrolysis-GC-MS traces for the linear (A) and branched (B) nickel xanthates with labels for the main compound peaks. Derived degradation product profiles for the linear (C) and branched (D) nickel xanthates. Cycloalkane* (D) was found only for the NiXaC5b precursor.

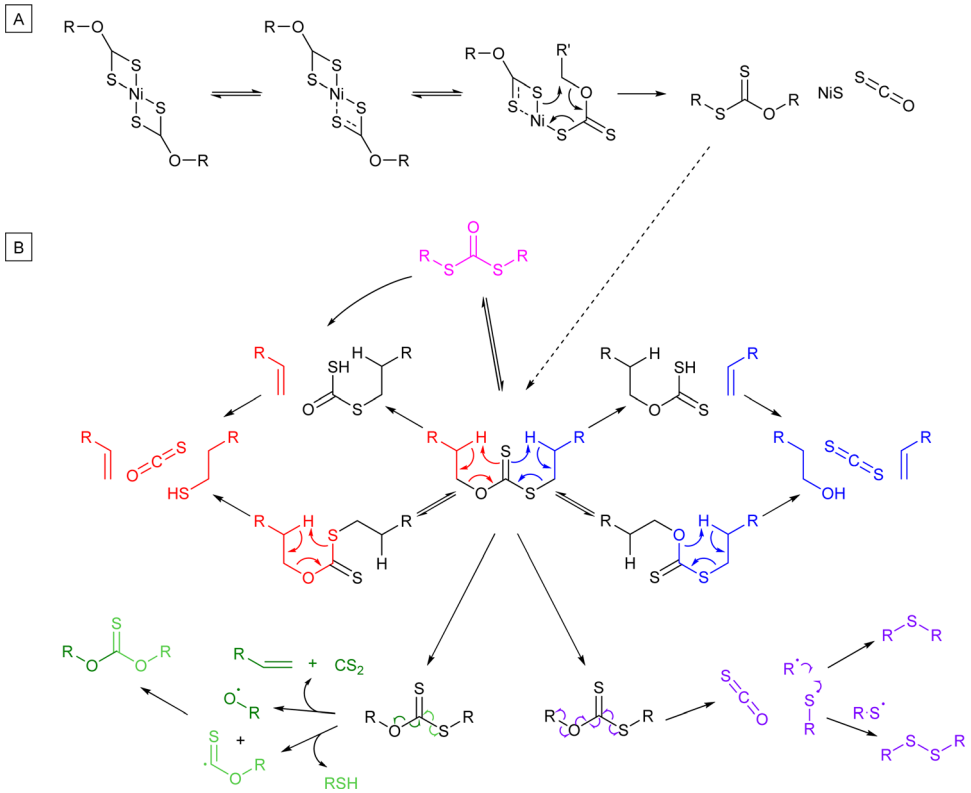

Scheme 4 Proposed decomposition pathway for nickel xanthates, proceeding *via* a two-step mechanism. Firstly, nickel sulfide and an organic xanthate ester are formed by an intramolecular alkyl transfer starting from the bidentate coordination mode of the xanthate ligands (A), secondly, followed by the decomposition of the xanthate ester (B). The classical and expanded Chugaev mechanism are drawn in red and blue, respectively. Other possible decomposition pathways include isomerization (pink) or radical formation and recombination (green and lilac).

6-membered transition state (Scheme 4A). The alkyl transfer eliminates the need for a β-hydrogen to be present in the structure. This explains the decomposition profile of the nickel methyl xanthate being consistent with the series of linear xanthates despite not having a β-hydrogen. In addition, it might provide an explanation for the different behavior of the branched ligand xanthates. The higher steric demand of the branched alkyl chain might hinder the attack of the sulfur atom on the α-carbon of the second xanthate ligand, therefore slowing the reaction and enabling another pathway. The steric pressure on the α-carbon (Scheme 3B) increases in the order NiXaC4b < NiXaC5b < NiXaC3b, which fits to the decrease of the relative amount of dithiocarbonate. Also, the branched precursor with the lowest steric hindrance (NiXaC4b) shows a decomposition profile matching that of the linear xanthates.

Not only are the obtained results contradictory to the pathway generally assumed to occur in literature reports, they also strongly differ from the results using the TGA-GC-MS setup (Fig. 4). For this comparison, we chose the linear pentyl xanthate NiXaC5, as its decomposition products are well resolved in the GC. The most noticeable difference is the prominent peak present in the pyrolysis-GC-HRMS measurement corresponding to the *O*,*S*-dipentyl dithiocarbonate (marked in yellow), which is only weakly existent in the TGA-GC-MS experiment. Instead, the TGA-GC-MS shows several medium intensity peaks (marked in black), with the main products being the dipentyl sulfide and pentane thiol. In addition, the expected Chugaev elimination product – 1-pentene – is present in relative high amounts compared to the pyrolysis-GC-HRMS measurement.

We conducted a series of follow up experiments with the TGA-GC-MS setup to investigate these discrepancies, using the precursor NiXaC5. For those experiments, the sample was heated rapidly to the sampling temperature, followed by an isothermal step during which the sampling for the GCMS occurred. The sampling temperature was varied between 200 and 250 °C. In addition, we adjusted the temperatures of the transfer system to the GC (transfer line, interface, and inlet) accordingly. For temperatures between 200 and 220 °C, the pentyl dithiocarbonate was the main decomposition product by far, while only small amounts of alkene, alcohol and thiol were detected. The product distribution resembles very much the results from the pyrolysis-GC-MS experiment. However, when increasing the sampling temperature to 230 °C, the amount of dithiocarbonate abruptly decreased, and we observed larger amounts of COS, alkene, and alcohol. Upon further increase of the temperature, we could no longer detect any significant amount of dithiocarbonate. Instead, larger amounts of alkene, carbon disulfide, aldehyde and alcohol were formed (Fig. 5). These findings, in combination with the previous results from the pyrolysis-GC-HRMS experiments, suggest that the decomposition of the metal xanthate occurs in two distinct steps. The

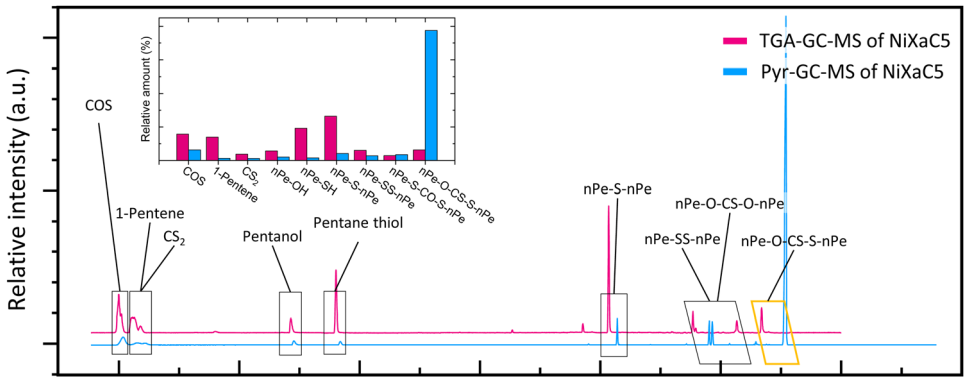

Fig. 4 Traces of the TGA-GC-MS (pink) and pyrolysis-GC-HRMS (blue) measurements of the precursor NiXaC5 with marked degradation products. The main decomposition product found for most xanthates in the pyrolysis-GC-HRMS experiments is marked in yellow. The scale of the x-axis was adjusted to compensate for the different GC columns to allow the visual comparison of the degradation profiles. Inset: Comparison of the relative amounts of the degradation products.

first step of the decomposition reaction is the formation of the metal sulfide and the *O*,*S*-dialkyl xanthate ester (Fig. 5A, 200 °C). The subsequent decomposition of the dialkyl xanthate ester occurs according to the Chugaev pathway and yields CS_2, COS, alkene, aldehyde, alcohol, thiol, and alkyl sulfides/disulfides (Fig. 5A, 250 °C).

In standard TGA-GC-MS experiments, the temperatures of the transfer system are set to higher values to minimize material deposition and clogging in the transfer line. However, this drastically changed the product distribution and complicated the identification of the degradation mechanism. We assumed that the high temperature in the transfer line resulted in the further decomposition of the unstable intermediates. To verify this assumption, we conducted another measurement at a low sampling temperature of 200 °C but kept the temperature of the GC components at 300 °C (Fig. 5A, 200*). This experiment showed a completely different decomposition profile, with low amounts of the dithiocarbonate and high amounts of the lighter products, thereby supporting our assumption. The direct comparison of the two main products for all the sampling temperatures is given in Fig. 5B.

Based on our results, we propose a combined decomposition pathway for the linear nickel xanthates and NiXaC4b (Scheme 4), assuming an intramolecular reaction mechanism. First, the nickel xanthate undergoes an alkyl transfer from one ligand to another, thereby forming a purely organic xanthate ester and nickel sulfide (Scheme 4A). The second step of the mechanism is the degradation of the organic xanthate *via* an expanded Chugaev mechanism (Scheme 4B). This includes the classical Chugaev mechanism (Scheme 4B, red), yielding alkene, COS,

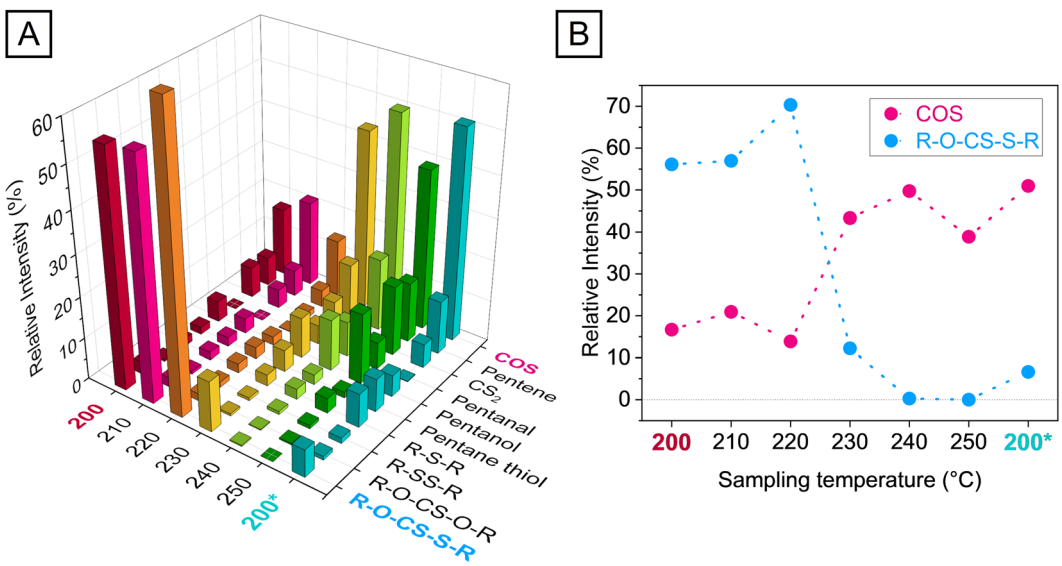

Fig. 5 (A) Results of the TGA-GCMS measurement of NiXaC5 at sampling- and instrument temperatures between 200 and 250 °C (order of the decomposition products was inverted compared to Fig. 3 for readability). The measurement denoted by 200* (turquoise) depicts a measurement at a sampling temperature of 200 °C and device transfer temperature of 300 °C. The comparison with the measurement 200 (dark red) illustrated the strong impact of the measurement conditions on the result. (B) Change of the relative amounts of the two main products (pink: COS, blue: dithiocarbonate) in dependence on the sampling- and instrument temperature.

and thiol. Additionally, it includes the possibility of the 6-membered transition state of the Chugaev pathway being formed *via* the hydrogen on the β-carbon to the xanthate sulfur (Scheme 4B, blue). This explains the presence of CS_2 and alcohol in the decomposition products. Further products can be explained by thermal rearrangement (Scheme 4B, pink), which yields the *S*,*S*-dialkyl xanthate, or the recombination of thermally formed radicals. Recombination leads to the formation of alkyl sulfides and disulfides (Scheme 4B, lilac), as well as the *O*,*O*-dialkylthiocarbonate (Scheme 4B, green).

While the decomposition profile of the branched precursor NiXaC4b matches those of the linear xanthates, NiXaC3b and NiXaC5b behave differently. For NiXaC5b the dialkyl dithiocarbonate is still the main decomposition product, but is present in a significantly lower percentage. This might be due to the steric hindrance of the large alkyl substituent, which slows down the proceeding of the intramolecular alkyl transfer, and possibly enables the occurrence of an alternative decomposition mechanism. A possibility for this might be a Chugaev-like decomposition mechanism consisting of the initial elimination of one alkyl substituent which forms the 1,1-dimethylcyclopropane. This is followed by the elimination of COS and the second xanthate ligand. For NiXaC3b, the decomposition profile suggests that the decomposition proceeds preferentially *via* a radical pathway.

Preparation and characterization of nickel sulfide thin films and powders

X-ray diffraction. Thin film samples of the various nickel xanthates were converted to NiS at different temperatures in a nitrogen atmosphere. For this purpose, thin films of the precursors were prepared by drop casting solutions of the precursors in chloroform onto glass slides. The samples were sintered on a heating plate in nitrogen atmosphere for 30 minutes at different temperatures (heating plate set to 200, 220, 250, 300, 350 and 400 °C). The XRD results for the thin film samples for 220 °C and 400 °C are given in Fig. 6, all other diffractograms can be found in Fig. S17 (ESI†). Afterwards, they were left on the heating plate until cooled to room temperature, thus a relatively slow cooling occurs. From the NiXaC1 precursor, no thin film XRD patterns could be obtained due to its low solubility. Additionally, powder samples were prepared using the same setup and conversion temperatures. In this case, larger amounts of the solid xanthate powders were placed directly onto glass substrates.

The obtained XRD patterns (Fig. 6) confirm the formation of NiS for all precursors and reveal a strong influence of the temperature and some influence of the side chain on the formed polymorph. Using an annealing temperature of 400 °C or 300 °C (see Fig. S17, ESI†) depending on precursor and temperature, mixtures of different ratios of the hexagonal α-NiS (main diffraction peaks: 30.1 (100), 45.9° 2θ (102)) and the rhombohedral β-NiS (main diffraction peaks: 18.5 (110), 32.2 (300), 48.9° 2θ (131/311)) were obtained.

However, an annealing temperature lower than 250 °C leads to the formation of pure α-NiS from all the precursors. Depending on the precursor, annealing at 200 °C is not sufficient for a complete conversion (C3, C4b, C5b, C6b, C7b, see Fig. S17 in ESI,† compare to TGA in Fig. 2). This formation of the α-NiS phase represents a reversal of the behavior typically reported for the Ni-S system: the thermodynamically stable β-NiS is formed at low temperatures, while the metastable α-NiS is only formed at high temperatures.[47] The presence of α-NiS at this relatively low temperature is a known peculiarity of the synthesis of NiS from sulfur-rich single-source precursors such as xanthates or dithiocarbamates.[19] Due to the high sulfur content in the system, xanthates favor the formation of the slightly over stochiometric, sulfur-rich α-phase.[48] Upon further heating, a phase transition from α- to β-NiS occurs, which can be observed in the emerging of the reflections of the beta phase, while the peaks corresponding to the alpha phase decrease in intensity.

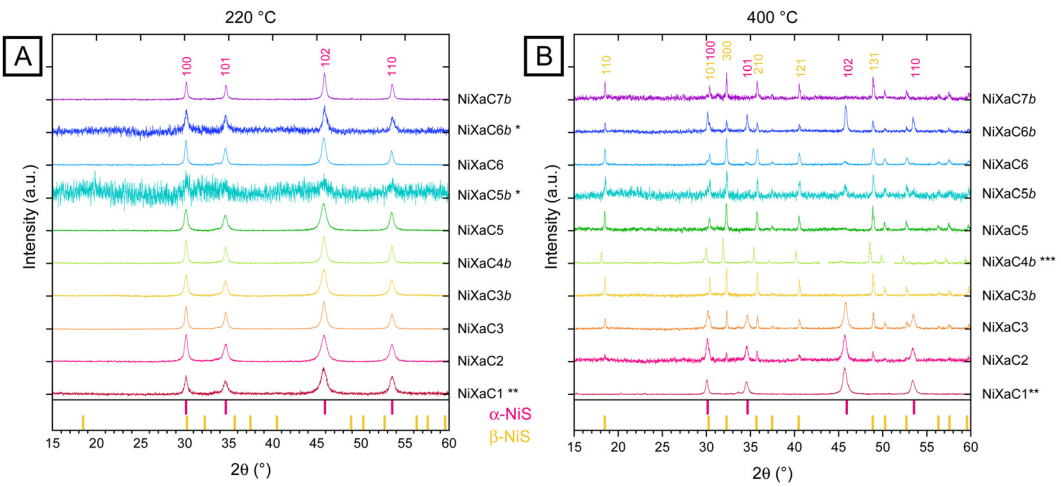

Fig. 6 XRD patterns of the different NiXa precursors after sintering at 220 °C (A) and 400 °C (B), N_2; with references for α-NiS (pink, PDF 01-075-0613, major reflection: 102, 45.9° 2θ) and β-NiS (yellow, PDF 01-086-2280, major reflections: 300, 32.2° 2θ/313, 48.8° 2θ) given below. The measurements NiXaC5b* and NiXaC6b* were conducted at 250 °C. NiXaC1** was measured as powder XRD. For NiXaC4b*** the trace is slightly shifted due to a slight misalignment of the sample during the measurement.

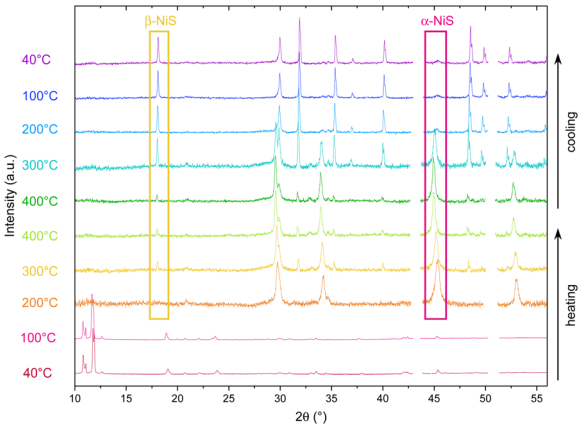

Fig. 7 XRD heating run of the precursor NiXaC4b. Heating rate: 2 °C min^{-1}, 30 minutes holding steps at 400 °C during heating and at 40 °C after cooling.

At 400 °C, varying mixtures of β- and α-NiS are obtained depending on the precursor. The amounts and the average crystallite sizes were calculated from the respective phase's major peaks (45.9 (102, α-NiS) and 32.2° 2θ (300, β-NiS), Tables S11 and S12, ESI†). For the short-chained precursors NiXaC2 and NiXaC3, the mixtures contained high amounts of α-NiS, while phase-pure β-NiS was formed from the precursors NiXaC4b, NiXaC5 and NiXaC7b. This possibility to control the phase plays an important role in tailoring materials properties to the desired application, such as photocatalysis.[49]

The formed polymorph is not only influenced by the sintering temperature, but also by other factors such as the heating rate. We did XRD heating runs of the precursor NiXaC4b to get real-time information of the thermal conversion and phase formation. When using a slow heating rate (Fig. 7), again, the formation of the α-phase can be observed initially. Subsequently, the β-phase emerges already during the heating step. During cooling, the α-phase is almost completely converted to the β-phase when reaching 200 °C. In contrast, when a fast heating rate is used, no β-phase is formed during the heating and holding step at 400 °C (Fig. S18A, ESI†). Only during cooling the α-phase is converted to β-NiS. Fast heating yields slightly smaller primary crystallites and a higher amount of α-NiS (see Fig. S18, ESI†).

However, the precursor also influences the product: a comparison of heating runs of two different precursors (NiXaC4b and NiXaC5b, Fig. S18 and S19, ESI†) at the same conditions shows that while both precursors yield a phase mixture, the NiS produced from the precursor NiXaC5b consists of predominantly α-NiS with significantly smaller primary crystallites.

Time resolved grazing incidence wide angle X-ray scattering

For a more detailed characterization of the NiS formation, we performed temperature dependent grazing incidence wide-angle X-ray scattering (GIWAXS) experiments using synchrotron radiation. We heated thin films of the xanthates on silicon substrates from 35 °C up to 400 °C under nitrogen flow, held at this temperature for 20 minutes, followed by cooling to room temperature. Fig. 8 depicts the heating runs for the two precursors yielding the most phase pure nickel sulfides, NiXaC3b (β-NiS) and NiXaC5b (α-NiS). 2D GIWAXS pictures for the selected temperatures (Fig. S20, ESI†) and additional heating runs for the precursors NiXaC2, NiXaC3 and NiXaC4b (Fig. S21–S23) are given in the ESI.†

In Fig. 8A, at low temperatures, the diffraction pattern of the crystalline NiXaC3b precursor is visible, which disappears at approximately 115 °C due to the melting of the precursor. At 170 °C, the alpha phase starts to emerge, which fits the onset-temperature of the decomposition determined by TGA (see Fig. 2). The presence of the alpha phase – usually considered the high-temperature phase – at this relatively low temperature can be explained by the aforementioned high sulfur content in the system.[48] Upon further heating, the reflections of the beta phase start to appear at 215 °C, while the ones corresponding to the alpha phase decrease in intensity. At 400 °C the alpha phase has disappeared almost completely. During the holding and cooling step, the primary crystallite size and crystallinity increase without further observable changes of the phase (Fig. 8B). From this precursor, NiS is obtained almost phase pure as β-NiS (α-NiS/β-NiS: 5.0/95.0%, calculated from the respective phase's major peaks at 45.9 (102, α-NiS) and 32.2° 2θ (300, β-NiS)).

For the nickel neopentyl precursor (Fig. 8C), the larger side chain leads to a higher stability, and the melting and onset of the decomposition can be observed at 200 and 210 °C, respectively. The reflections of the alpha phase start to emerge shortly after at 215 °C. Interestingly, further heating did not lead to a phase transition, only an increase of the primary crystallite size (Fig. 8D), forming significantly larger crystallites than when the α-NiS exists as the minor phase (Fig. 8B). This differs from the XRD measurement of the thin films prepared on glass slides (Fig. 6B), which shows a high percentage of β-NiS. As phase transitions in nanomaterials can be influenced by many different interacting factors,[19] these variations could be due to differences in the experimental setups of XRD and GIWAXS measurements, such as nitrogen flow and heating rates. In addition, the formed phase can also be influenced by the support material (for this measurement silicon), as reported by Buchmaier *et al.*[22]

The previous experiments have been carried out in thin films, however, we observed similar trends in NiS prepared as powders (Fig. 9). The β-NiS phase remains the major phase for the precursors NiXaC3b, NiXaC4b and NiXaC7b, while most other precursors lead to phase mixtures. Due to the different heat distribution and cooling in the bulk phase compared to thin films, different phase ratios are obtained.

Conclusion

In this study, we synthesized and characterized a series of nickel xanthates carrying ligands with linear or branched alkyl chains of varying lengths. From those xanthate precursors, we prepared nickel sulfide in a simple thermal degradation

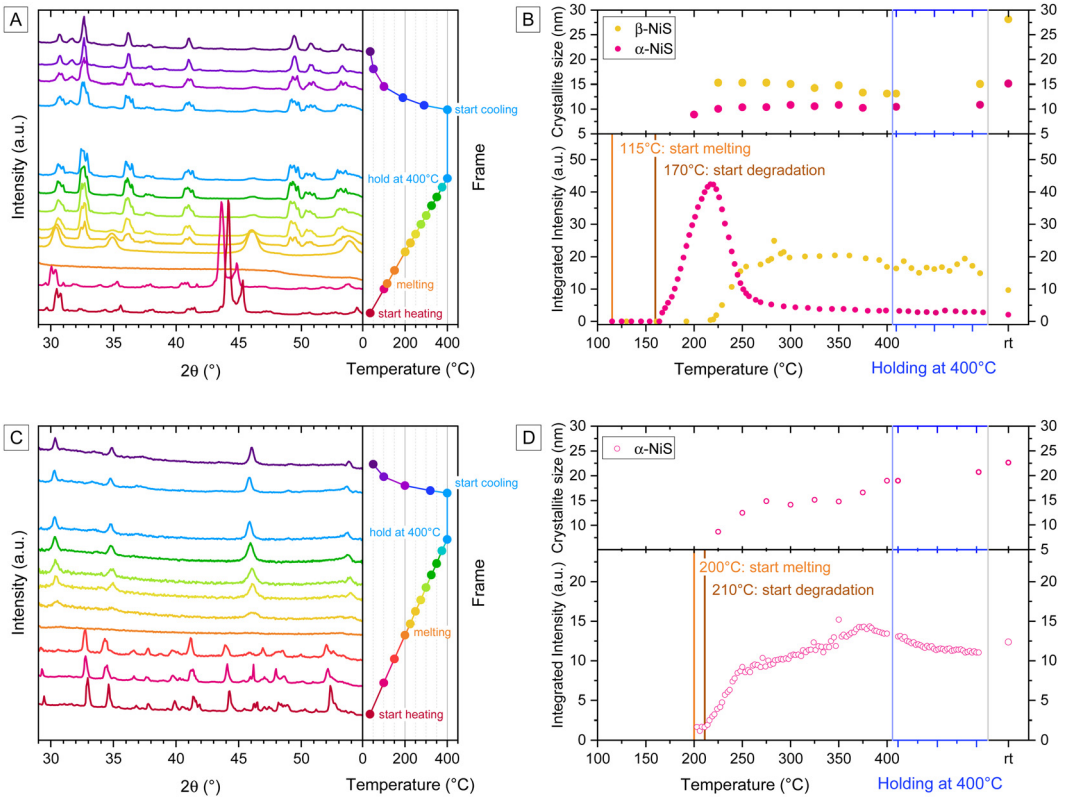

Fig. 8 (A) Selected curves of the GIWAXS heating run for the precursor NiXaC3b. Peaks appear significantly broadened due to the large cross section of beam and sample in the grazing incidence setup. (B) Change of the integrated intensity in the out-of-plane direction (bottom) and the primary crystallite size (top) with the temperature for the major reflections of α-NiS (45.9° 2θ, pink) and β-NiS (32.2° 2θ, yellow), the start of the melting range of the precursor NiXaC3b (115 °C) is marked in orange. (C) Selected curves of the GIWAXS heating run for the precursor NiXaC5b. (D) Change of the integrated intensity (bottom) and primary crystallite size (top) with the temperature for α-NiS, start of the melting range of the precursor NiXaC5b (200 °C) marked in orange.

reaction under nitrogen atmosphere, studied their conversion behavior and the properties of the synthesized NiS nanoparticles and thin films. We were able to shed light on the degradation mechanism, which was generally assumed to occur according to the Chugaev mechanism. For the investigated nickel xanthates, however, we discovered a range of decomposition products which cannot be explained by this mechanism. This finding is also reflected in a certain inconsistency in the reports published so far. Therefore, we propose a different mechanism which proceeds *via* two steps: in the first step, the nickel xanthate is converted to NiS and a purely organic xanthate carrying both alkyl side chains. Only in the second step, a degradation of the organic xanthate according to a Chugaev-like mechanism occurs, alongside a radical side reaction. This two-step mechanism also illustrates the importance of having a good understanding on how strongly measurement parameters can influence the observations: when choosing a too high temperature, the individual steps of the mechanism cannot be resolved. Hence, our experimental findings and proposed mechanism bridges the conflicting reports of degradation products that are published so far. One of the studied precursors (NiXaC3b) differentiates from the trend nicely discernible for the other precursors. This, as well as an assessment if this degradation behavior is common to other metal xanthates will be interesting for further investigations.

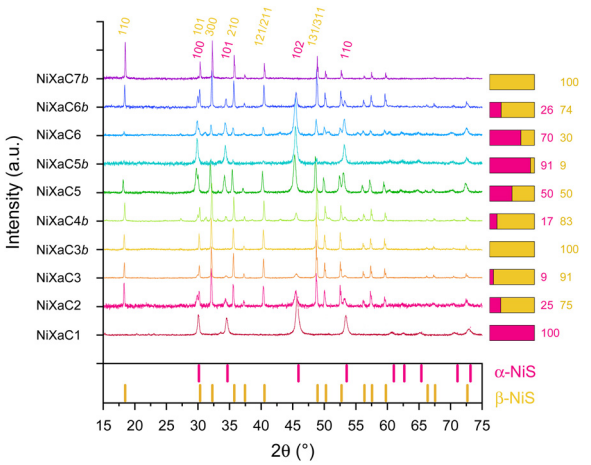

Fig. 9 Powder XRD measurements of the different NiXa precursors after sintering at 400 °C, N_2; with references for α-NiS and β-NiS given below. Right: Ratio of α-NiS and β-NiS estimated from the intensities of the major reflections of the respective phases (α-NiS: (102), 45.9° 2θ, β-NiS: (300), 32.2° 2θ/(313), 48.8° 2θ).

In the second part of this study, we investigated the formation of the NiS phases from the precursors. While it is

obvious that there are several factors influencing the final phase composition, we were able to show that for all precursors, α-NiS is the initial phase. At higher temperatures, the α-phase is partly or fully converted to β-NiS for most precursors. Slow heating generally resulted in a more complete conversion of the α- to the β-NiS phase for precursors yielding a phase mixture, and the formation of larger primary crystallites. So, although we could not determine the underlying reasons, it was possible to reproducibly obtain phase-pure α- or β-NiS and mixtures of both phases, depending on precursor choice and heating rates.

Our findings enabled us (i) to propose a refined degradation mechanism for nickel xanthates and (ii) to a good extent, control the formed nickel sulfide polymorph. Further research regarding the influence of the alkyl chains on properties such as porosity, particle sizes and more will be of interest for applications. Xanthates as single-source precursors provide a very facile and increasingly used method to prepare homogeneous nanomaterials and thin films of semiconductors, with possible applications ranging from printable electronics to photovoltaics and electro- or photocatalysis.

Experimental section

All chemicals and solvents were used as purchased without any additional purification: chloroform (≥99.2%, VWR), diethyl ether (≥99.5%, Sigma-Aldrich), acetone (≥99%, Sigma-Aldrich), deuterium oxide (Eurisotop), deuterated chloroform (99.8 atom% D, 0.03% (v/v) TMS, Eurisotop), carbon disulfide (≥99.9%, Sigma-Aldrich), nickel chloride hexahydrate (Sigma-Aldrich), potassium hydroxide (Roth), methanol (≥99.9%, VWR), ethanol (99%, In-house), 2-propanol (99.9%, Sigma-Aldrich), 1-propanol (99%, VWR), 2-butanol (99%, VWR), 1-pentanol (≥99%, Sigma-Aldrich), neopentyl alcohol (99%, Thermo Scientific), 1-hexanol (≥99%, Sigma-Aldrich).

Nickel *O*-3,3-dimethylbutan-2-yl-dithiocarbonate (NiXaC6b) and nickel *O*-2,2-dimethylpentan-3-yl-dithiocarbonate (NiXaC7b) were previously prepared.[22] Potassium ethyl xanthate was purchased from Sigma-Aldrich and used without further purification.

NMR spectra were recorded on a Bruker Ultrashield 300 MHz NMR spectrometer (^{1}H NMR: 300 MHz, ^{13}C NMR: 75 MHz). The solvents used were deuterated chloroform with tetramethylsilane (TMS) (^{1}H NMR: 7.26 ppm, ^{13}C NMR: 77.16 ppm) and deuterium oxide (^{1}H NMR: 4.79 ppm). The spectra were evaluated with TopSpin 3.1 from Bruker.

FTIR spectra were measured on a Bruker Alpha FTIR spectrometer in attenuated total reflection (ATR) mode using the ALPHA's Platinum ATR single-reflection diamond ATR module. All spectra were recorded in a range between 4000 and 400 cm^{-1} with 24 scans and the air as background.

Thermogravimetric measurements were performed on a PerkinElmer TGA 8000 thermogravimetric analyzer in ceramic crucibles under nitrogen atmosphere with a flow rate of 40 mL min^{-1}. The operated temperature range was between 40–450 °C with heating rates of 10 to 40 °C min^{-1}. The onset of decomposition temperature was taken as the intersection of the baseline and the tangent at the point of maximum gradient.

Thermogravimetric measurements with coupled gas chromatography/mass spectrometry (TGA-GCMS) were performed on a GCMS-QP2010 SE equipped with a GC-2010 Plus from Shimadzu (Kyoto, Japan) and the GC column Zebron ZB-5ms (30 m, 0.25 mm i.d., 0.25 mm film thickness) from Phenomenex (Torrance, CA/USA). The sample was introduced to the GC *via* a transfer line from the TGA. The GC was operated with nitrogen as carrier gas at a flow of 0.5 mL min^{-1}. The program of the oven was: Initial temperature of 40 °C for 4 min, heating to 300 °C at 20 °C min^{-1} and holding at this temperature for 5 minutes. Mass spectra were acquired after a solvent delay of 0.2 min in the mass range of 35–600 m z^{-1} with a recording interval of 0.2 s.

Pyrolysis gas chromatography/mass spectrometry (Pyrolysis-GCMS) analyses were performed on a JMS-T2000GC (AccuTOF™ GC-Alpha) from JEOL Ltd (Tokyo, Japan) equipped with an 8890 GC System from Agilent (Santa Clara, CA/USA) and a Single-Shot Pyrolyzer PY-3030S from Frontier Laboratories Ltd (Saikon, Koriyama, Japan). The furnace temperature of the pyrolyzer (T_{Pyr}) was usually 250 °C, the interface temperature 250 °C, and a sampling time of 0.1 min was applied. The GC column used was a Zebron ZB-5 ms (30 m, 0.25 mm i.d., 0.25 mm film thickness) from Phenomenex (Torrance, CA/USA). The GC was operated with helium as carrier gas at a constant flow rate of 1.0 mL C min^{-1}, the split ratio was 10. The program of the oven was as follows: Initial temperature of 40 °C for 3 min, heating to 280 °C at a rate of 20 °C min^{-1}, and finally isothermal at 280 °C for 5 min. The GC-MS interface was at 270 °C. Electron ionization (EI$^+$, 70 eV, 200 μA; source at 250 °C) mass spectra were acquired after a solvent delay of 0.2 min in the mass range 10–700 Da using a recording interval of 0.25 s. The resolution (FWMH) was >16 000 for small masses, and >30 000 at higher *m*/*z* ratios. Mass calibration was done with PFTBA, drift compensation *via* reference from the reservoir in time windows of 0.6–0.8 and 19.6–9.8 min, respectively.

Appr. 0.1 μg of the samples were filled into the deactivated sample cup of the pyrolyzer and transferred into the pyrolyzer. To allow removal of oxygen brought into the system with the sample/cup pyrolysis-GC-MS analysis were started after an additional delay of 5 min using the conditions described above.

Data analysis/chromatographic deconvolution was done with the software msFineAnalysis version 2 from JEOL. All detected peaks were searched against the NIST 2020 mass spectral database. Elemental composition analysis was performed for molecular ions as well as for all corresponding fragment ions. Mass accuracies were generally in the low ppm range (compare tables in the ESI†).

X-ray diffraction (XRD) measurements were taken on a RIGAKU MiniFlex 600 with D/Tex Ultra detector operated at 40 kV and 15 mA using CuKα radiation (λ = 1.5418 Å). The measurement was performed on a silicon zero-background sample holder.

Grazing incidence wide angle X-ray scattering (GIWAXS) measurements were performed at the Austrian SAXS beamline

5.2 L of the electron storage ring Elettra (Italy).[50] The GIWAXS setup was adjusted for an angular range of 2θ between 29 and 55° ($q = 4\pi/\lambda\sin(2\theta/2)$) and the experiments were carried out with a photon energy of 8 keV. The angular calibration of the used Pialtus3 100 K detector was performed using *p*-bromo benzoic acid. The conversion of the diffraction images was conducted with SAXSDOG.[51] The samples were mounted on an Anton Paar DHS 1100 heating cell equipped with a specially designed dome with Kapton windows to provide high X-ray transmissivity with low background. The sample chamber was purged with N_2 during the heating run experiments. One frame was recorded every 6 seconds for a temperature resolution of 1 °C and an incident angle of 0.55° was used.

For the determination of the integrated intensity (out-of-plane direction) of the α- and β-NiS in the heating runs, reflexes without overlapping neighbor peaks were chosen. NiXaC3b: 2θ values of 44.7 to 47.5° (102, α-phase), 48.6 to 49.9° (300, β-phase). NiXaC5b: 2θ values of 45.3 to 46.8° (102, α-phase).

For single crystal X-ray crystallography, all crystals suitable for single crystal X-ray diffractometry were removed from a vial and immediately covered with a layer of silicone oil. Compounds NiXaC3, NiXaC3b, NiXaC4b, NiXaC5b, NiXaC6 crystallized as a birefringent crystal (dichroic) with the colors light orange/green. A single crystal was selected, mounted on a mitegen on a copper pin, and placed in the cold N_2 stream provided by an Oxford Cryosystems cryostream. Data for crystal structures of the aforementioned compounds were collected using a Rigaku XtaLAB Synergy, Dualflex, HyPix-Arc 100 diffractometer. Data were measured using Cu Kα radiation (λ = 1.54056 Å). The diffraction pattern was indexed and the total number of runs and images was based on the strategy calculation from the program CrysAlisPro.[52] The unit cell was refined and data reduction, scaling and absorption corrections were performed using CrysAlisPro. Using Olex2,[53] the structure was solved with the SHELXT[54] structure solution program and refined with the SHELXL[55] refinement package using full matrix least squares minimization on F^2. All non-hydrogen atoms were refined anisotropically. All hydrogen atoms for all compounds were located in the difference map. All crystal structures representations were made with the program Diamond[56] with all non-carbon atoms displayed as 30% ellipsoids. CIF files were edited, validated and formatted either with the programs encifer,[57] publCIF,[58] or Olex2.[53] All presented C–H···S hydrogen bonds[22] and C–H···Ni anagostic interactions[59–61] fall within expected ranges. Compound NiXaC3[42] has been previously published. The crystal structures NiXaC3b,[43] NiXaC4b,[37] NiXaC6[37] had been reported at RT, therefore, the 100 K data obtained for these structures were deposited in the CCDC database along with the newly reported NiXaC5b. CCDC 2430036–2430039 contain the supplementary crystallographic data for the compounds NiXaC3b, NiXaC4b, NiXaC5b and NiXaC6, respectively. These data can be obtained free of charge from The Cambridge Crystallographic Data Centre *via* www.ccdc.cam.ac.uk/data_request/cif. Table S14 (ESI†) contains crystallographic data and details of measurements and refinement.

Synthesis of potassium xanthates

Potassium *O*-alkyl-dithiocarbonate (KXaCx). Potassium *O*-alkyl dithiocarbonates were synthesized for further use in the nickel xanthate synthesis. The compounds were synthesized according to a previous procedure.[33] Finely ground potassium hydroxide (1 equiv.) was dissolved in the corresponding alcohol in slight to moderate surplus (1.1 equiv. for short chain alcohols, up to 3 equiv. for long chain alcohols (C5, C6)). The solution was then cooled down to 0 °C and stirred until most of the potassium hydroxide was dissolved, then CS_2 (1.1 equiv.) was added dropwise. The reaction mixture was stirred for 3 h, followed by precipitation of the product by adding diethyl ether and collection by filtration. The dry product was purified by recrystallization from acetone and precipitation with diethyl ether. The white to yellowish solid was collected by filtration and dried under vacuum.

Potassium *O*-methyl-dithiocarbonate (KXaC1). FT-IR (cm^{-1}): 2988, 2932, 2826, 2813, 1699, 1448, 1429, 1185, 1085, 1040, 942, 576, 471. Yield: 45%.

Potassium *O*-propyl-dithiocarbonate (KXaC3). ^{1}H-NMR (300 MHz, D_2O): δ = 4.43 (t, 2H, OCH_2), 1.825–1.754 (sext, 2H, CH_2), 1.00 (t, 3H, CH_3) ppm. FT-IR (cm^{-1}): 2971, 2927, 2870, 1585, 1461, 1371, 1265, 1180, 1145, 1127, 1050, 900, 690, 461. Yield: 50%.

Potassium *O*-isopropyl-dithiocarbonate (KXaC3b). ^{1}H-NMR (300 MHz, D_2O): δ = 5.48–5.56 (m, 1H, OCH), 1.32–1.34 (d, 6H, 2×CH_3) ppm. FT-IR (cm^{-1}): 2957, 2928, 2870, 1462, 1386, 1367, 1244, 1181, 1165, 1140, 1090, 1070, 968, 913, 838, 802, 498. Yield: 50%.

Potassium *O*-isobutyl-dithiocarbonate (KXaC4b). ^{1}H-NMR (300 MHz, D_2O): δ = 4.20–4.23 (d, 2H, OCH_3), 1.98–2.11 (m, 1H, CH), 0.93-0.96 (d, 6H, 2×CH_3) ppm. FT-IR (cm^{-1}): 2961, 2929, 2872, 1460, 1389, 1367, 1180, 1165, 1143, 1090, 1073, 968, 915, 801497. Yield: 42%.

Potassium *O*-pentyl-dithiocarbonate (KXaC5). ^{1}H-NMR (300 MHz, D_2O): δ = 4.39–4.43 (t, 2H, OCH_2), 1.71–1.75 (m, 2H, CH_2), 1.34–1.35 (m, 4H, 2×CH_2), 0.85–0.90 (t, 3H, CH_3) ppm. FT-IR (cm^{-1}): 2958, 2923, 2857, 1458, 1378, 1250, 1211, 1136, 1064, 776, 747, 581, 504. Yield: 45%.

Potassium *O*-hexyl-dithiocarbonate (KXaC6). ^{1}H-NMR (300 MHz, D_2O): δ = 4.41–4.45 (t, 2H, OCH_2), 1.69–1.78 (m, 2H, CH_2), 1.37–1.42 (m, 4H, 2×CH_2), 1.30–1.33 (m, 2H, CH_2), 0.85–0.89 (t, 3H, CH_3) ppm. FT-IR (cm^{-1}): 2951, 2919, 2853, 1465, 1375, 1233, 1135, 1069, 893, 726, 534, 505, 443. Yield: 43%.

Potassium *O*-neopentyl-dithiocarbonate (KXaC5b). Potassium *O*-neopentyl-dithiocarbonate (KXaC5b) was synthesized using a slightly modified synthesis procedure. Finely ground potassium hydroxide (1 equiv.) was suspended in THF and stirred for 30 minutes. Neopentanol (1.1 equiv.) was dissolved in THF and added to the mixture. The solution was then cooled down to 0 °C and stirred for 15 minutes, followed by the dropwise addition of CS_2 (1.1 equiv.). The reaction mixture was stirred overnight at room temperature, the product was worked up and purified as before, resulting in a crystalline white product. ^{1}H-NMR (300 MHz, D_2O): δ = 4.14 (s, 2H, CH_2), 0.97 (s, 9H, 3×CH_3) ppm. FT-IR (cm^{-1}): 2965, 2867, 1451, 1363,

1215, 1108, 1080, 1061, 1026, 963, 912, 881, 767, 702, 669, 475. Yield: 57%.

Synthesis of nickel xanthates

Nickel(II) *O*-alkyl-dithiocarbonate (NiXaCx). The compound was synthesized following an adapted procedure reported previously.[22] An aqueous solution of the corresponding potassium xanthate (2.1 equiv.) was slowly added to an aqueous solution of nickel(II) chloride (1.0 equiv.) under ambient conditions. The reaction mixture was stirred for 2 h. The green solid was filtered off, washed with distilled water, and dried under vacuum. For recrystallization, the dry product was dissolved in chloroform and filtered, concentrated using a rotary evaporator until the first crystals formed, and fully precipitated by adding methanol, yielding dark green crystals.

Nickel (II)-*O*-methyl-dithiocarbonate (NiXaC1). ^{1}H-NMR (300 MHz, $CDCl_3$): δ = 4.13 (s, 3H, OCH_3) ppm, ^{13}C-NMR (75 MHz, $CDCl_3$): solubility too low. FT-IR (cm^{-1}): 2991, 2936, 2836, 1447, 1430, 1232, 1171, 1079, 1034, 947, 620, 547, 455. Yield: 80%.

Nickel(II)-*O*-ethyl-dithiocarbonate (NiXaC2). ^{1}H-NMR (300 MHz, $CDCl_3$): δ = 4.53–4.60 (q, 2H, OCH_2), 1.43–1.48 (t, 3H, CH_3) ppm, ^{13}C-NMR (75 MHz, $CDCl_3$): δ = 231.3 (CS_2O), 68.5 (OCH_2), 13.8 (CH_3) ppm. FT-IR (cm^{-1}): 2983, 2936, 2854, 2891, 1465, 1430, 1389, 1365, 1325, 1253, 1145, 1112, 1059, 1020, 996, 855, 808, 663, 553, 435. Yield: 75%.

Nickel(II)-*O*-propyl-dithiocarbonate (NiXaC3). ^{1}H-NMR (300 MHz, $CDCl_3$): δ = 4.44–4.48 (t, 2H, OCH_2), 1.82–1.89 (m, 2H, CH_2), 0.99–1.04 (t, 3H, CH_3) ppm, ^{13}C-NMR (75 MHz, $CDCl_3$): δ = 231.5 (CS_2O), 73.9 (OCH_2), 21.6 (CH_2), 10.2 (CH_3) ppm. FT-IR (cm^{-1}): 2966, 2934, 2875, 1467, 1396, 1375, 1310, 1261, 1234, 1140, 1128, 1032, 930, 890, 757, 667, 555, 469. Yield: 49%.

Nickel(II)-*O*-isopropyl-dithiocarbonate (NiXaC3b). ^{1}H-NMR (300 MHz, $CDCl_3$): δ = 5.38-5.47 (m, 1H, OCH), 1.43–1.45 (d, 6H, 2×CH_3) ppm, ^{13}C-NMR (75 MHz, $CDCl_3$): δ = 230.3 (CS_2O), 78.1 (OCH), 21.6 (CH_3) ppm. FT-IR (cm^{-1}): 2977, 2930, 2865, 2612, 1603, 1462, 1444, 1375, 1353, 1275, 1183, 1143, 1077, 1010, 896, 802, 655, 559, 457. Yield: 42%.

Nickel(II)-*O*-isobutyl-dithiocarbonate (NiXaC4b). ^{1}H-NMR (300 MHz, $CDCl_3$): δ = 4.26–4.28 (d, 2H, OCH_2), 2.08-2.22 (m, 1H, CH), 0.99-1.02 (d, 6H, 2×CH_3) ppm, ^{13}C-NMR (75 MHz, $CDCl_3$): δ = 231.5 (CS_2O), 78.1 (OCH_2), 27.7 (CH), 18.8 (CH_3) ppm. FT-IR (cm^{-1}): 29959, 2924, 2866, 1459, 1393, 1375, 1338, 1304, 1265, 1179, 1155, 1130, 1094, 1038, 953, 922, 898, 830, 755, 667, 557, 479, 437. Yield: 78%.

Nickel(II)-*O*-pentyl-dithiocarbonate (NiXaC5). ^{1}H-NMR (300 MHz, $CDCl_3$): δ = 4.47–4.51 (t, 2H, OCH_2), 1.79–1,81 (m, 2H, CH_2), 1.37–1.38 (m, 4H, CH_2), 0.90–0.95 (t, 2H, CH_3) ppm, ^{13}C-NMR (75 MHz, $CDCl_3$): δ = 231.4 (CS_2O) 72.6 (OCH_2), 27.8 (CH_2), 27.7 (CH_2), 22.2 (CH_2), 13.9 (CH_3) ppm. FT-IR (cm^{-1}): 2958, 2928, 2864, 2852, 1463, 1398, 1379, 1360, 1261, 1202, 1124, 1055, 1024, 987, 867, 775, 745, 730, 663, 553, 492, 475, 426. Yield: 70%.

Nickel(II)-*O*-neopentyl-dithiocarbonate (NiXaC5b). ^{1}H-NMR (300 MHz, $CDCl_3$): δ = 4.16 (s, 2H, OCH_2), 1.02 (s, 9H, 3×CH_3) ppm, ^{13}C-NMR (75 MHz, $CDCl_3$): δ = 231.6 (CS_2O), 81.2 (OCH_2), 31.8 (C), 26.3 (CH_3) ppm. FT-IR (cm^{-1}): 2956, 2905, 2866, 1473, 1449, 1404, 1375, 1300, 1279, 1253, 1194, 1061, 1045, 1022, 945, 926, 904, 759, 659, 552, 496, 465. Yield: 75%.

Nickel(II)-*O*-hexyl-dithiocarbonate (NiXaC6). ^{1}H-NMR (300 MHz, $CDCl_3$): δ = 4.47-5.51 (t, 2H, OCH_2), 1.79–1.83 (m, 2H, CH_2), 1.38–1.43 (m, 4H, CH_2), 1.31–1.34 (m, 2H, CH_2), 0.88–0.93 (t, 3H, CH_3) ppm, ^{13}C-NMR (75 MHz, $CDCl_3$): δ = 231.5 (CS_2O), 72.6 (OCH_2), 31.3 (CH_2), 28.1 (CH_2), 25.3 (CH_2), 22.5 (CH_2), 14.0 (CH_3) ppm. FT-IR (cm^{-1}): 2952, 2933, 2914, 2865, 2849, 1467, 1396, 1378, 1344, 1295, 1263, 1155, 1129, 1080, 1043, 1020, 910, 888, 800, 748, 725, 670, 557, 491, 454. Yield: 65%.

Conversion of the precursors to nanocrystalline nickel sulfide

The conversion was performed in a glovebox under nitrogen atmosphere. The nickel xanthate precursors were spread on glass slides and placed on a CAT MCS 78 heating plate. The samples were heated to 400 °C for 30 min and then cooled down to room temperature. For all precursors except the NiXaC1 precursor, thin films of NiS were formed on the glass slides. From NiXaC1 no films could be prepared, the precursor yielded a crystalline powder.

Author contributions

M. E.: conceptualization, data curation, formal analysis, synthesis and investigation, characterization methodology, project administration, visualization, writing – original draft, writing – review & editing. M. S: conceptualization, data curation, investigation, writing – review & editing. R. S.: data curation & investigation (pyrolysis-GC-HRMS), writing – review & editing. H. A.: conceptualization, data curation & investigation (GIWAXS), writing – review & editing. A. T.: data curation & investigation (single-crystal X-ray analysis), writing – review & editing. T. R.: conceptualization, funding acquisition, supervision, writing – review & editing. G.T.: resources, conceptualization, funding acquisition, supervision, writing – review & editing.

Data availability

All evaluated data is available in the manuscript. The data supporting this article are included as part of the ESI.† Additional information/data can be provided upon reasonable request.

Conflicts of interest

There are no conflicts to declare.

Acknowledgements

The authors gratefully acknowledge the Graz University of Technology for financial support through the Lead Project Porous Materials at Work for Sustainability (LP-03). Additionally, the authors thank the CERIC-ERIC Consortium for the access to experimental facilities of the Austrian SAXS beamline at Elettra

Sincrotrone Trieste as well as financial support. The authors further thank Virginia Lafranconi and Lukas Troi for their help with the time resolved GIWAXS characterizations.

References

1 S. Chandrasekaran, L. Yao, L. Deng, C. Bowen, Y. Zhang, S. Chen, Z. Lin, F. Peng and P. Zhang, *Chem. Soc. Rev.*, 2019, **48**, 4178–4280.
2 H. Gu, Z. Lin, Y. Li, D. Wang and H. Feng, *Phys. Status Solidi A*, 2024, 2400187.
3 X. Liu, Y. Li, Z. Cao, Z. Yin, T. Ma and S. Chen, *J. Mater. Chem. A*, 2022, **10**, 1617–1641.
4 S. Deb and P. K. Kalita, *J. Mater. Sci.: Mater. Electron.*, 2021, **32**, 24125–24137.
5 N. Kim, W. Na, W. Yin, H. Jin, T. K. Ahn, S. M. Cho and H. Chae, *J. Mater. Chem. C*, 2016, **4**, 2457–2462.
6 X. Zhang, W. Guo, G. Gao, M. Que, C. Pan and Z. L. Wang, *J. Mater. Chem. C*, 2016, **4**, 4733–4739.
7 C.-H. Lai, M.-Y. Lu and L.-J. Chen, *J. Mater. Chem.*, 2012, **22**, 19–30.
8 F. Jamal, A. Rafique, S. Moeen, J. Haider, W. Nabgan, A. Haider, M. Imran, G. Nazir, M. Alhassan, M. Ikram, Q. Khan, G. Ali, M. Khan, W. Ahmad and M. Maqbool, *ACS Appl. Nano Mater.*, 2023, **6**, 7077–7106.
9 G. Xiang, Y. Meng, G. Qu, J. Yin, B. Teng, Q. Wei and X. Xu, *Sci. Bull.*, 2020, **65**, 443–451.
10 J. Huang, Z. Shi and X. Dong, *J. Energy Chem.*, 2016, **25**, 136–140.
11 C. Y. Toe, S. Zhou, M. Gunawan, X. Lu, Y. H. Ng and R. Amal, *J. Mater. Chem. A*, 2021, **9**, 20277–20319.
12 Y. Zhang, D. Yang, W. Guo, F. Zhang, H. Lin, K. Yu, C. Yang and F. Qu, *Dalton Trans.*, 2022, **51**, 6817–6824.
13 Z. Liu, H. Ding, L. Qi, J. Wang, Y. Li, L. Liu, G. Feng and L. Zhang, *ACS Appl. Mater. Interfaces*, 2023, **15**, 52276–52289.
14 A. Sharma, P. R. Makgwane, E. Lichtfouse, N. Kumar, A. H. Bandegharaei and M. Tahir, *Environ. Sci. Pollut. Res.*, 2023, **30**, 64932–64948.
15 C. Daulbayev, F. Sultanov, B. Bakbolat and O. Daulbayev, *Int. J. Hydrogen Energy*, 2020, **45**, 33325–33342.
16 H. Emadi, M. Salavati-Niasari and A. Sobhani, *Adv. Colloid Interface Sci.*, 2017, **246**, 52–74.
17 I. M. Germaine and L. McElwee-White, *Cryst. Growth Des.*, 2024, **24**, 1–16.
18 M. A. Malik, M. Afzaal and P. O'Brien, *Chem. Rev.*, 2010, **110**, 4417–4446.
19 G. B. Shombe, M. D. Khan, C. Zequine, C. Zhao, R. K. Gupta and N. Revaprasadu, *Sci. Rep.*, 2020, **10**, 3260.
20 P. S. Nair, T. Radhakrishnan, N. Revaprasadu, G. Kolawole and P. O'Brien, *J. Mater. Chem.*, 2002, **12**, 2722–2725.
21 A. Piquette, Oklahoma State University, Stillwater, Oklahoma, 2007.
22 C. Buchmaier, M. Glänzer, A. Torvisco, P. Poelt, K. Wewerka, B. Kunert, K. Gatterer, G. Trimmel and T. Rath, *J. Mater. Sci.*, 2017, **52**, 10898–10914.
23 M. Sigl, M. Egger, F. Warchomicka, D. Knez, M. Dienstleder, H. Amenitsch, G. Trimmel and T. Rath, *J. Mater. Chem. A*, 2024, **12**, 28965–28974.
24 S. A. Alderhami, D. Collison, D. J. Lewis, P. D. McNaughter, P. O'Brien, B. F. Spencer, I. Vitorica-Yrezabal and G. Whitehead, *Dalton Trans.*, 2019, **48**, 15605–15612.
25 S. A. Saah, M. D. Khan, J. A. M. Awudza, N. Revaprasadu and P. O'Brien, *J. Inorg. Organomet. Polym. Mater.*, 2019, **29**, 2274–2281.
26 N. Alam, M. S. Hill, G. Kociok-Köhn, M. Zeller, M. Mazhar and K. C. Molloy, *Chem. Mater.*, 2008, **20**, 6157–6162.
27 T. Lutz, A. MacLachlan, A. Sudlow, J. Nelson, M. S. Hill, K. C. Molloy and S. A. Haque, *Phys. Chem. Chem. Phys.*, 2012, **14**, 16192.
28 T. Rath, M. Edler, W. Haas, A. Fischereder, S. Moscher, A. Schenk, R. Trattnig, M. Sezen, G. Mauthner, A. Pein, D. Meischler, K. Bartl, R. Saf, N. Bansal, S. A. Haque, F. Hofer, E. J. W. List and G. Trimmel, *Adv. Energy Mater.*, 2011, **1**, 1046–1050.
29 E. Vakalopoulou, T. Rath, M. Kräuter, A. Torvisco, R. C. Fischer, B. Kunert, R. Resel, H. Schröttner, A. M. Coclite, H. Amenitsch and G. Trimmel, *ACS Appl. Nano Mater.*, 2022, **5**, 1508–1520.
30 P. D. McNaughter, S. A. Saah, M. Akhtar, K. Abdulwahab, M. A. Malik, J. Raftery, J. A. M. Awudza and P. O'Brien, *Dalton Trans.*, 2016, **45**, 16345–16353.
31 M. A. Buckingham, K. Norton, P. D. McNaughter, G. Whitehead, I. Vitorica-Yrezabal, F. Alam, K. Laws and D. J. Lewis, *Inorg. Chem.*, 2022, **61**, 8206–8216.
32 M. Al-Shakban, P. D. Matthews, G. Deogratias, P. D. McNaughter, J. Raftery, I. Vitorica-Yrezabal, E. B. Mubofu and P. O'Brien, *Inorg. Chem.*, 2017, **56**, 9247–9254.
33 E. Vakalopoulou, C. Buchmaier, A. Pein, R. Saf, R. C. Fischer, A. Torvisco, F. Warchomicka, T. Rath and G. Trimmel, *Dalton Trans.*, 2020, **49**, 14564–14575.
34 P. D. McNaughter, J. Moore, S. G. Yeates and D. J. Lewis, *ACS Appl. Energy Mater.*, 2024, **2**, 1225–1233.
35 A. J. MacLachlan, T. Rath, U. B. Cappel, S. A. Dowland, H. Amenitsch, A. Knall, C. Buchmaier, G. Trimmel, J. Nelson and S. A. Haque, *Adv. Funct. Mater.*, 2015, **25**, 409–420.
36 E. A. Lewis, P. D. McNaughter, Z. Yin, Y. Chen, J. R. Brent, S. A. Saah, J. Raftery, J. A. M. Awudza, M. A. Malik, P. O'Brien and S. J. Haigh, *Chem. Mater.*, 2015, **27**, 2127–2136.
37 M. J. Cox and E. R. T. Tiekink, *Z. Kristallogr. - Cryst. Mater.*, 1999, **214**, 242–250.
38 K. J. Cavell, C. G. Sceney, J. O. Hill and R. J. Magee, *Thermochim. Acta*, 1973, **5**, 319–328.
39 P. A. Kotei, N. O. Boadi, S. A. Saah and M. B. Mensah, *Adv. Mater. Sci. Eng.*, 2022, 1–10.
40 A. V. Ivanov, O. A. Bredyuk, O. N. Antzutkin and W. Forsling, *Russ. J. Coord. Chem.*, 2004, **30**, 480–485.
41 W. Friebolin, G. Schilling, M. Zöller and E. Amtmann, *J. Med. Chem.*, 2005, **48**, 7925–7931.
42 L. C. Juncal, E. G. Ferrer, P. A. M. Williams, R. Boese, C. G. Pozzi, C. O. Della Védova and R. M. Romano, *Chem. Phys. Lett.*, 2022, **794**, 139487.

43 M. J. Cox and E. R. T. Tiekink, *Z. Kristallogr. - Cryst. Mater.*, 1996, **211**, 111–113.
44 Y. Y. Lim and K. L. Chua, *J. Chem. Soc., Dalton Trans.*, 1975, 1917.
45 B. F. Hoskins, E. R. T. Tiekink and G. Winter, *Z. Kristallogr. - Cryst. Mater.*, 1985, **172**, 257–262.
46 N. Pradhan, B. Katz and S. Efrima, *J. Phys. Chem. B*, 2003, **107**, 13843–13854.
47 O. Yousfi, P. Donnadieu, Y. Bréchet, F. Robaut, F. Charlot, A. Kasper and F. Serruys, *Acta Mater.*, 2010, **58**, 3367–3380.
48 Y. Zhang, H. Yuan, Z. Liu, C. Wang, W. Kong, L. Xu, Y. Sun, M. Zhang and S. Tan, *J. Mater. Sci.: Mater. Electron.*, 2023, **34**, 1328.
49 J. Yi, Y. Xia, Z. Zhou, G. Zhou, X. Zhu, S. Zhang, X. Zhu, X. Wang, H. Xu and H. Pang, *Inorg. Chem. Front.*, 2023, **10**, 5917–5926.
50 H. Amenitsch, M. Rappolt, M. Kriechbaum, H. Mio, P. Laggner and S. Bernstorff, *J. Synchrotron Radiat.*, 1998, **5**, 506–508.
51 M. Burian, C. Meisenbichler, D. Naumenko and H. Amenitsch, *arXiv*, 2020, preprint, DOI: **10.48550/arxiv.2007.02022**.
52 CrysAlisPro Software System, 1.171.43.92a; Rigaku Oxford Diffraction: 2023 (version 1.171.43.92a).
53 O. V. Dolomanov, L. J. Bourhis, R. J. Gildea, J. A. K. Howard and H. Puschmann, *J. Appl. Crystallogr.*, 2009, **42**, 339–341.
54 G. M. Sheldrick, *Acta Crystallogr., Sect. A*, 2015, **71**, 3–8.
55 G. M. Sheldrick, *Acta Crystallogr., Sect. A*, 2008, **64**, 112–122.
56 H. Putz and K. Brandenburg, H. Putz; K. Brandenburg, Diamond - Crystal and Molecular Structure Visualization, 4.6.5; Crystal Impact: Bonn, Germany. (version 4.6.5) Crystal Impact, Bonn, Germany.
57 F. H. Allen, O. Johnson, G. P. Shields, B. R. Smith and M. Towler, *J. Appl. Crystallogr.*, 2004, **37**, 335–338.
58 S. P. Westrip, *J. Appl. Crystallogr.*, 2010, **43**, 920–925.
59 M. K. Yadav, G. Rajput, L. B. Prasad, M. G. B. Drew and N. Singh, *New J. Chem.*, 2015, **39**, 5493–5499.
60 E. Sathiyaraj, P. Selvaganapathi, S. Thirumaran and S. Ciattini, *J. Mol. Struct.*, 2016, **1119**, 385–395.
61 A. Husain, S. A. A. Nami, S. P. Singh, M. Oves and K. S. Siddiqi, *Polyhedron*, 2011, **30**, 33–40.